The Journal of Green Energy and Environmental Engineering

Research Paper

Characterization of Schiff Base Modified MCM-41 Molecular Sieve for Adsorption of Lead Ions from Aqueous Solution

Kwame Nkrumah[1], Luca Ferrari[2,*]

[1] College of Pharmacy, University of Cambridge, United Kingdom
[2] The York Management School, University of York, Heslington, York, YO10 5DD, UK
*Corresponding author: KNkrumah323@cam.ac.uk; Ferrari2015@york.ac.uk

Abstract. A new Schiff base modified MCM-41 molecular sieve (N-MCM-41) was synthesized via a post-grafting method using 2-pyridine formaldehyde as the Schiff base ligand to achieve efficient adsorption of lead ions (Pb^{2+}) from aqueous solutions. The structure, morphology, surface functional groups, and chemical states of N-MCM-41 were analyzed using X-ray diffraction (XRD), scanning electron microscopy (SEM), transmission electron microscopy (TEM), Fourier-transform infrared spectroscopy (FT-IR), thermogravimetric analysis (TGA), and X-ray photoelectron spectroscopy (XPS). The adsorption behavior of N-MCM-41 toward Pb^{2+} in aqueous solution was systematically investigated. The maximum adsorption capacity of this adsorbent for Pb^{2+} reached 101.3 mg/g. The adsorption behavior of Pb^{2+} by N-MCM-41 conformed to the pseudo-second-order kinetic model and the Langmuir isotherm model, indicating that the adsorption process was spontaneous and endothermic. The chelation and coordination between the surface functional groups of N-MCM-41 and Pb^{2+} were identified as the primary mechanism for removing Pb^{2+} from water. After five regeneration cycles, N-MCM-41 retained favorable adsorption performance, demonstrating promising application prospects for the treatment of lead-contaminated water bodies.

Keywords: *MCM-41 molecular sieves; Schiff base; Modification; Adsorption; Lead ion*

Received on 02 March 2023, Accepted on 28 May 2023, Published on 15 July 2023

1 Introduction

Lead is one of the most abundant heavy metal elements on Earth, widely present in environmental systems such as air, soil, and water. However, lead ions (Pb^{2+}) are highly toxic; they can enter the human body through food ingestion or respiration and accumulate within it, leading to various diseases such as anemia, genotoxicity, and cancer [1–2]. Particularly with the rapid development of industry, substantial amounts of lead-containing industrial pollutants are discharged into water bodies, causing severe water pollution. Therefore, there is an urgent need to develop efficient and economical methods for removing Pb^{2+} from water.

In recent years, researchers have proposed various methods to mitigate the environmental hazards of heavy metal ions, including adsorption [3], redox methods [4], electrochemical methods [5], bioflocculation [6], and bioremediation [7]. Among these methods, adsorption is regarded as the most promising water treatment technology due to its low cost, environmental friendliness, and operational simplicity. The selection of adsorbent materials directly affects the adsorption efficiency of heavy metal ions. Common adsorbent materials include activated carbon [8], sodium alginate [9], graphene oxide [10], resins [11], and molecular sieves [12]. However, the adsorption capacities of the aforementioned untreated materials for heavy metal ions fall far short of practical requirements. Chemical methods are typically employed to graft organic functional groups onto their surfaces, enabling coordination and chelation with heavy metal ions in solution to achieve effective removal.

Consequently, identifying suitable organic functional groups is crucial for enhancing the adsorption performance of adsorbents toward heavy metal ions. Schiff bases are organic compounds containing imine or methanimine characteristic groups (-RC=N-), which act as electron donors to form stable complexes with heavy metal ions. Leveraging the coordination and chelation capability of Schiff base functional groups with heavy metal ions, they can be grafted onto the surface of adsorbent materials to improve adsorption performance, providing an effective technical route for preparing heavy metal ion adsorbents [13]. Zhang et al. [14] utilized a Schiff base reaction to graft salicylaldehyde onto the surface of SBA-15 mesoporous molecular sieves, preparing a functionalized silica material capable of efficiently adsorbing Pb^{2+} from wastewater. Liang et al. [15] modified SBA-15 mesoporous molecular sieves using 4-methylthiazole as a Schiff base ligand, obtaining an adsorbent with excellent Pb^{2+} adsorption performance. However, the high preparation cost of SBA-15 mesoporous molecular sieves restricts their practical application in water treatment. MCM-41 molecular sieves, as a low-cost mesoporous silica material, are widely used in adsorption and separation fields due to their large pore sizes, high specific surface area, and good chemical and thermal stability [16]. Nevertheless, studies on the removal of Pb^{2+} using Schiff base-modified MCM-41 mesoporous molecular sieves are rarely reported.

In this study, 2-pyridine formaldehyde was grafted onto MCM-41 mesoporous molecular sieves via a Schiff base reaction to prepare a novel Schiff base-modified MCM-41 molecular sieve (N-MCM-41). Effective adsorption of Pb^{2+} was achieved by utilizing the synergistic coordination effect of the -C=N- groups in the Schiff base structure and the nitrogen atoms in the pyridine ring on the surface of N-MCM-41. The morphology, structure, elemental distribution, and surface functional groups of N-MCM-41 were systematically investigated using various characterization techniques, and the adsorption behavior of N-MCM-41 toward Pb^{2+} in aqueous solution was analyzed in detail.

2 Experimental Section

2.1 Instruments and Reagents

DF-101S thermostatic magnetic stirrer (Gongyi Yuhua Instrument Co., Ltd.); BSA124S electronic balance (Sartorius Scientific Instruments (Beijing) Co., Ltd.); 101-00B electric blast drying oven (Shaoxing Supo Instrument Co., Ltd., Zhejiang); SHZ-D(III) circulating water vacuum pump (Shanghai Lichen Bangxi Instrument Technology Co., Ltd.); SRJX-3-12 muffle furnace (Shenyang General Electric Furnace Manufacturing Co., Ltd.).

Tetraethyl orthosilicate (TEOS), cetyltrimethylammonium bromide (CTAB), NaOH, anhydrous ethanol, HCl, and $Pb(NO_3)_2$ (analytical grade, Tianjin Kemiou Chemical Reagent Co., Ltd.); 2-pyridine formaldehyde (analytical grade, Hebei Bailingwei Ultra-Fine Materials Co., Ltd.); 3-aminopropyltrimethoxysilane (APTMS) and glacial acetic acid (analytical grade, Sinopharm Chemical Reagent Co., Ltd.).

2.2 Experimental Methods

2.2.1 Preparation of 2-Pyridine Formaldehyde Modified MCM-41 Adsorbent

The synthetic route for the 2-pyridine formaldehyde modified MCM-41 adsorbent is illustrated in Fig. 1.

2.4 g of CTAB was dissolved in 120 mL of ultrapure water and stirred until the solution became clear. Subsequently, 10.25 mL of ammonia solution (25%, m/V) was added, and the mixture was stirred for 10 min. Then, 10 mL of TEOS was added dropwise to the above mixed solution and stirred overnight. The resulting white suspension was transferred into a stainless-steel autoclave and crystallized in an oven at 110 °C for 24 h. The obtained sample was calcined in a muffle furnace at 500 °C for 6 h to yield MCM-41 mesoporous molecular sieves.

Next, 2.5 g of MCM-41 molecular sieves was dispersed in a flask containing 150 mL of anhydrous ethanol and stirred for 10 min. Then, 2.5 mL of APTMS solution was added to the flask, and the mixture was refluxed under a nitrogen atmosphere for 24 h. After the reaction, the mixture was cooled to room temperature, washed repeatedly with anhydrous ethanol, suction-filtered, and dried to obtain amino-modified MCM-41 molecular sieves, denoted as NH_2-MCM-41.

Finally, 1.0 g of NH_2-MCM-41 was dispersed in 60 mL of anhydrous ethanol, and 1.0 mL of 2-pyridine formaldehyde was added. After stirring uniformly, 3–4 drops of glacial acetic acid were added dropwise. The mixture was refluxed under a nitrogen atmosphere for 24 h. After the reaction, the product was washed repeatedly with anhydrous ethanol, suction-filtered, and dried to obtain the 2-pyridine formaldehyde modified MCM-41 molecular sieve, denoted as N-MCM-41.

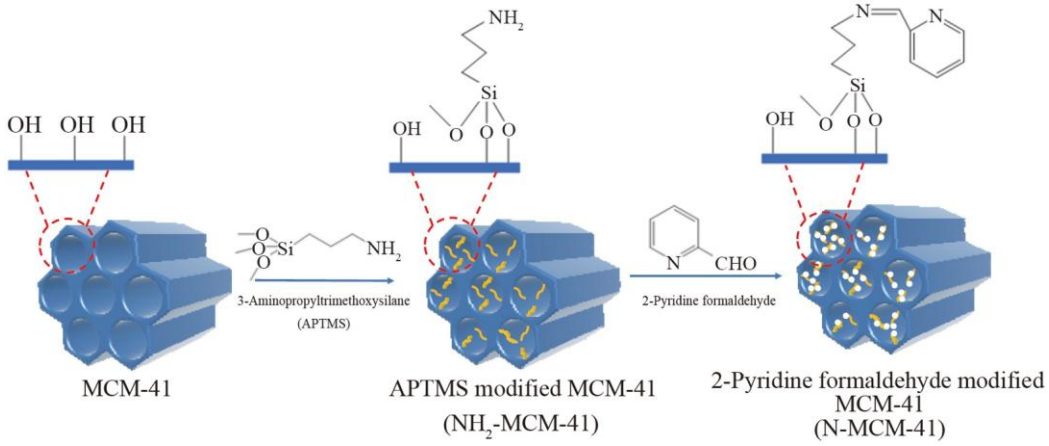

Figure 1 Schematic diagram of synthetic process of Schiff base modified MCM-41 molecular sieve (N-MCM-41)

2.2.2 Sample Characterization

The surface morphology of the samples was analyzed using a Hitachi S-4800 field emission scanning electron microscope (FESEM, Hitachi). The microstructure was observed using a JEM 2010 transmission electron microscope (TEM, JEOL). Functional groups on the sample surfaces were determined using a VERTEX 70 Fourier-transform infrared spectrometer (FT-IR, Bruker). Thermal stability was measured using an STA 449C thermogravimetric analyzer (TGA, Netzsch). Surface elemental binding energies were analyzed using an ESCALAB-250Xi X-ray photoelectron spectrometer (XPS, Thermo Scientific). Crystal structures were analyzed using a D/Max 2400 X-ray diffractometer (XRD, Rigaku). Specific surface areas were determined using an ASAP 2460 gas adsorption instrument (BET, Micromeritics).

2.2.3 Adsorption Experiments

50 mL of $Pb(NO_3)_2$ solution with a specific concentration was transferred into a 100 mL conical flask, and 15 mg of the N-MCM-41 adsorbent was added. The mixture was stirred in a constant-temperature water bath for a set period. After centrifugation, the supernatant was collected, and the concentration of Pb^{2+} was measured using a 240DUO atomic absorption spectrometer (Agilent, USA). The adsorption capacity was calculated according to Formula (1).

$$q=(C0-C)\times V/m$$

Where q(mg/g) is the adsorption capacity of Pb^{2+}, V(mL) is the volume of the Pb^{2+} solution, C0 (mg/L) is the initial mass concentration of Pb^{2+}, C(mg/L) is the mass concentration of Pb^{2+} after adsorption, and m(g) is the mass of the adsorbent.

3 Results and Discussion

3.1 Characterization of Adsorbents

Fig. 2A and 2C show the SEM images of MCM-41 and N-MCM-41 molecular sieves, respectively. As shown in Fig. 2A, the synthesized MCM-41 molecular sieves exhibit spherical and rod-like aggregated morphologies, which

are typical characteristics of MCM-41 [17]. After modification with 2-pyridine formaldehyde, the morphology of N-MCM-41 showed no significant change (Fig. 2C). The TEM images (Fig. 2B and 2D) reveal that the N-MCM-41 molecular sieve retains the typical two-dimensional hexagonal pore structure of MCM-41 [18], with ordered and regular pore channels. EDX elemental analysis (Fig. 2E) confirms that the surface of N-MCM-41 contains not only C, O, and Si elements but also N elements, preliminarily verifying the successful introduction of 2-pyridine formaldehyde onto N-MCM-41.

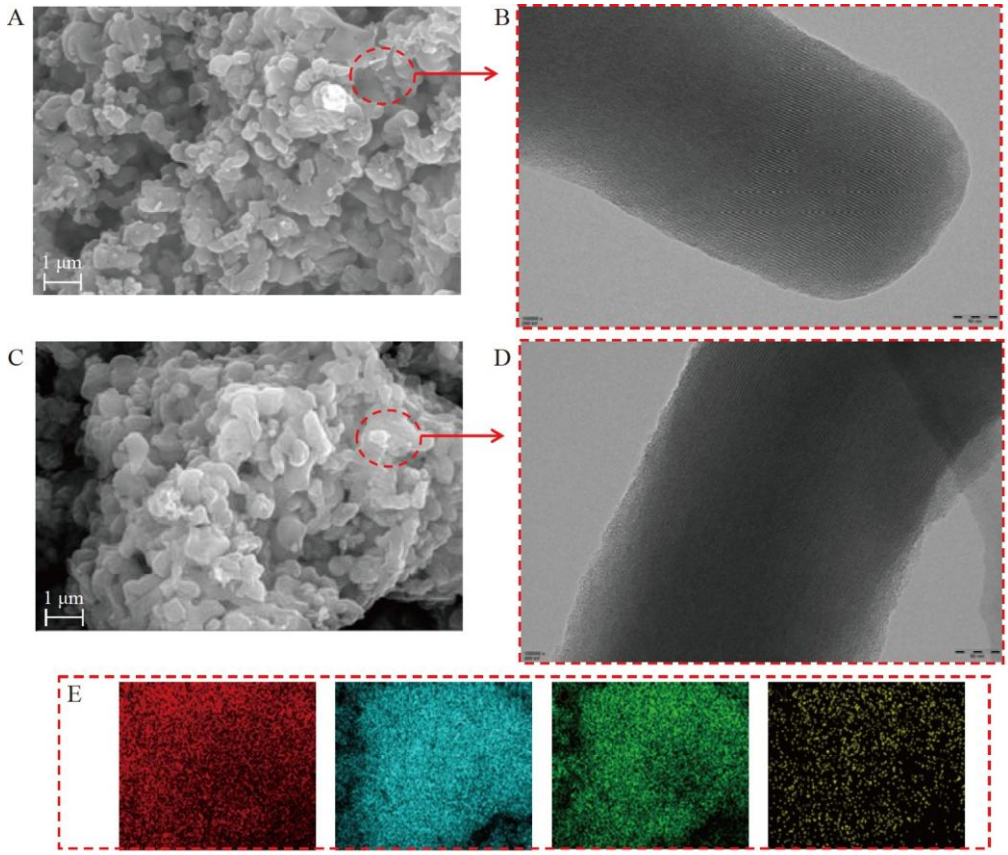

Figure 2 Scanning electron microscopy (SEM) images (A, C), transmission electron microscopy (TEM) images (B, D) and energy dispersive X-ray (EDX) mapping analyses (E) of MCM-41 and N-MCM-41.

XRD was employed to analyze the crystal structure of MCM-41 before and after modification. As shown in Fig. 3A, N-MCM-41 exhibits distinct diffraction peaks at 2θ values of 2.20°, 3.79°, and 4.39°, corresponding to the (100), (110), and (200) crystal planes, respectively. This indicates a high degree of pore order, consistent with the typical two-dimensional hexagonal structure (p6mm) of MCM-41 molecular sieves [19]. The aforementioned morphological and structural analyses suggest that the introduction of 2-pyridine formaldehyde onto MCM-41 via the Schiff base reaction did not affect the inherent morphology and mesoporous structure of the MCM-41 molecular sieves.

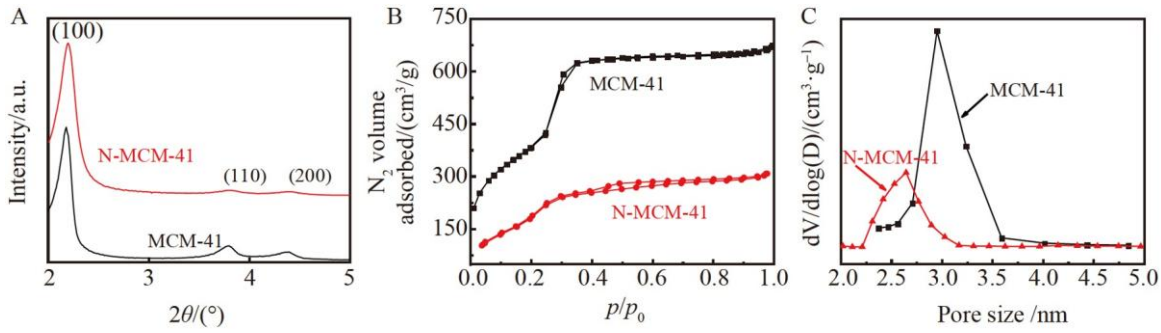

Figure 3 X-ray diffraction (XRD) patterns (A), N_2 adsorption-desorption isotherms (B) and pore size distribution (C) of MCM-41 and N-MCM-41.

Fig. 3B and 3C display the N_2 adsorption-desorption isotherms and pore size distribution curves of the samples, respectively. As shown in Fig. 3B, both MCM-41 and N-MCM-41 exhibit type IV isotherms and H1-type hysteresis loops characteristic of mesoporous materials [20], which is consistent with the XRD results. Using the BJH model, the specific surface area, pore volume, and average pore size of the MCM-41 molecular sieve were calculated to be 1392.92 cm^2/g, 1.02 cm^3/g, and 2.95 nm, respectively. Compared with MCM-41, the N_2 adsorption capacity of N-MCM-41 decreased significantly, and its specific surface area, pore volume, and average pore size were reduced to 734.10 cm^2/g, 0.43 cm^3/g, and 2.64 nm, respectively (Table 1). These results are primarily attributed to the grafting of 2-pyridine formaldehyde into the pores of N-MCM-41, which occupied the pore channels and affected the N_2 adsorption-desorption process.

Table 1 Textural properties of the synthesized samples.

Sample	SBET/ (m^2/g)	Pore volume / (cm^3/g)	Pore size / nm
MCM-41	1392.92	1.02	2.95
N-MCM-41	734.10	0.43	2.64

The XPS full survey spectrum of N-MCM-41 (Fig. 4A) shows characteristic peaks at binding energies of 153.5 eV (Si 2s), 102.0 eV (Si 2p), 284.5 eV (C 1s), 533.0 eV (O 1s), and 399.5 eV (N 1s), confirming the presence of N elements on the surface of the N-MCM-41 material, which is consistent with the EDX analysis results (Fig. 2E). Comparing the FT-IR spectra of MCM-41 and N-MCM-41 (Fig. 4B), several identical characteristic peaks are observed in both samples. Peaks at 802 cm^{-1} and 1087 cm^{-1} correspond to the symmetric [21] and asymmetric stretching vibrations of Si-O-Si [22], respectively; the peak at 461 cm^{-1} corresponds to the bending vibration of O-Si-O [23]; and the peak at 963 cm^{-1} corresponds to the stretching vibration of Si-OH. After modification with 2-pyridine formaldehyde, new characteristic peaks emerged in N-MCM-41. Peaks at 1442 cm^{-1}, 2982 cm^{-1}, and 1652 cm^{-1} are attributed to the scissoring vibration of $-CH_2-CH_2-$, the asymmetric stretching vibration of $-CH_2$ [24], and the characteristic vibration of C=N [25], respectively.

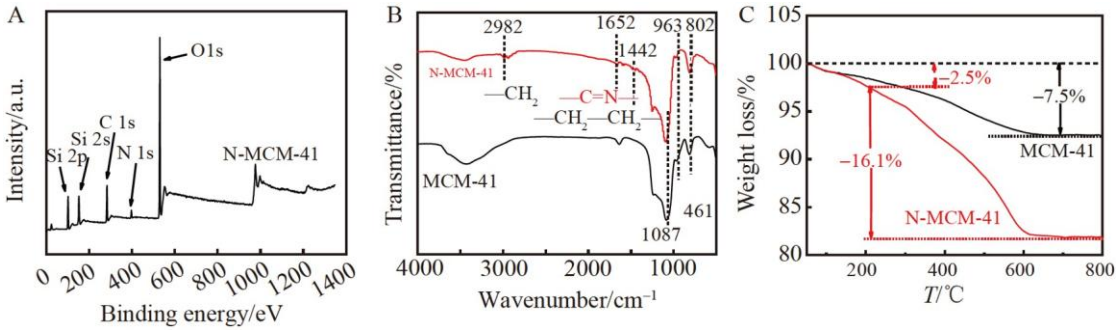

Figure 4 X-ray photoelectron spectroscopy (XPS) pattern of N-MCM-41 (A); Fourier transform-infrared (FT-IR) spectra (B) and thermogravimetric analysis (TGA) curves (C) of MCM-41 and N-MCM-41.

The TGA curves of MCM-41 and N-MCM-41 (Fig. 4C) show that within the range of 50–800 °C, MCM-41 experienced a weight loss of 7.5%. This is attributed to the desorption of water from the surface and pores of MCM-41 and the condensation of surface silanol groups into Si-O-Si bonds [26]. In contrast, the weight loss of N-MCM-41 increased significantly to 18.6%. Within the 50–200 °C range, a weight loss of 2.5% is attributed to the evaporation of water molecules from the sample surface and pores. Between 200 and 800 °C, the sample lost 16.1% of its weight, primarily due to the thermal decomposition of the organic functional groups grafted onto the surface of N-MCM-41. The aforementioned XPS, FT-IR, and TGA results collectively confirm the successful grafting of 2-pyridine formaldehyde onto the MCM-41 molecular sieve via the Schiff base reaction.

3.2 Adsorption Performance of N-MCM-41

3.2.1 Adsorption Isotherms

To investigate the interaction between N-MCM-41 and Pb^{2+}, the Langmuir (Formula (2)) and Freundlich (Formula (3)) isotherm models were employed to fit the obtained adsorption data.

$$\frac{C_e}{q_e} = \frac{C_e}{q_m} + \frac{1}{q_m K_L} \quad (2)$$

$$\ln q_e = \frac{\ln C_e}{n} + \ln K_F \quad (3)$$

Where Ce (mg/L) is the equilibrium concentration in solution, qe (mg/g) is the equilibrium adsorption capacity of Pb^{2+}, qm (mg/g) is the theoretical maximum adsorption capacity of Pb^{2+}, KL (L/mg) is the Langmuir adsorption equilibrium constant, KF (L/g) is the Freundlich adsorption equilibrium constant, and nis a constant related to adsorption intensity.

The effect of initial Pb^{2+} concentration on the adsorption performance of N-MCM-41 at different temperatures is shown in Fig. 5A. The dosage of N-MCM-41 was 15 mg, the solution pH was 5.5, the solution volume was 50 mL, and the adsorption time was 240 min. As shown in Fig. 5A, the adsorption capacity of N-MCM-41 for Pb^{2+} increased with rising temperature and increasing Pb^{2+} concentration, indicating that higher temperatures favor Pb^{2+} adsorption. When the Pb^{2+} concentration increased to 80 mg/L, adsorption reached equilibrium.

Fig. 5B and 5C present the fitting curves of the Freundlich and Langmuir adsorption isotherm models for N-MCM-41 at different temperatures, respectively, with the relevant fitting parameters listed in Table 2. Comparative analysis reveals that at temperatures of 293, 303, and 318 K, the correlation coefficients (R2) for the Langmuir model fitting were 0.998, 0.992, and 0.995, respectively, which are significantly higher than those for the Freundlich model (0.936, 0.922, and 0.947) at the same temperatures. Moreover, the theoretical maximum adsorption capacity (qm) derived from the Langmuir model closely matches the experimental values. These results indicate that the adsorption of Pb^{2+} by N-MCM-41 conforms to the Langmuir isotherm model, suggesting a monolayer adsorption process [27]. In this study, the KL values were all less than 1, indicating that the adsorption process of Pb^{2+} by N-MCM-41 is favorable [28].

Table 2 Simulated parameters for adsorption of Pb^{2+} by N-MCM-41 at different temperatures using different models

T / K	qe(exp)/ (mg/g)	KF/ (L/g)	n	R2(Freundlich)	qm/ (mg/g)	KL/ (L/mg)	R2(Langmuir)
298	62.67	36.618	8.196	0.936	65.40	0.248	0.998
308	80.67	41.010	6.561	0.922	82.71	0.245	0.992
318	101.33	46.609	5.484	0.947	106.95	0.220	0.995

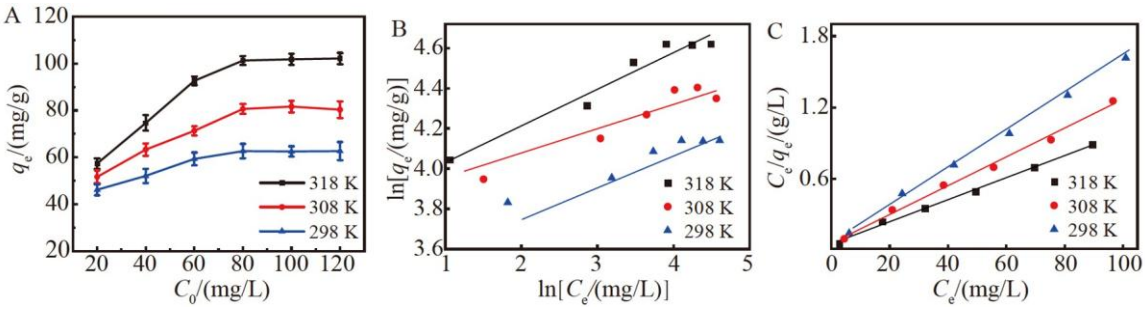

Figure 5 Effect of initial Pb^{2+} concentration on adsorption performance of N-MCM-41 (A); Simulated curves of Freundlich adsorption isotherm model (B) and Langmuir adsorption isotherm model (C).

3.2.2 Adsorption Kinetics

Fig. 6A shows the variation of Pb^{2+} adsorption capacity by N-MCM-41 over time. The dosage of N-MCM-41 was 15 mg, the Pb^{2+} concentration was 80 mg/L, the adsorption temperature was 318 K, and the solution pH was 5.5. As shown in Fig. 6A, within the range of 10–240 min, the adsorption capacity of N-MCM-41 for Pb^{2+} gradually increased with prolonged adsorption time. This is because, in the initial stage of the reaction, a large number of adsorption sites were available on the surface of N-MCM-41, and the high concentration of Pb^{2+} in the solution provided a high adsorption driving force, allowing the active sites on N-MCM-41 to rapidly coordinate with Pb^{2+}. When the adsorption time reached 180 min, the adsorption capacity remained essentially unchanged, reaching a value of 101.3 mg/g. This is attributed to the decreasing Pb^{2+} concentration in the solution over time, which reduces the adsorption driving force, coupled with the occupation of numerous active sites on the N-MCM-41 surface by Pb^{2+}, leading to adsorption equilibrium.

To further investigate the adsorption behavior and rate-controlling steps of Pb^{2+} adsorption by N-MCM-41, the pseudo-first-order kinetic model (Eq. (4)) and the pseudo-second-order kinetic model (Eq. (5)) were used to analyze the experimental data.

$$\ln(q_e - q_t) = \ln q_e - k_1 t \tag{4}$$

$$\frac{t}{q_t} = \frac{1}{k_2 q_e^2} + \frac{t}{q_e} \tag{5}$$

Where qt (mg/g) and qe (mg/g) are the adsorption amounts at time t(min) and at equilibrium, respectively; k1 (min^{-1}) is the equilibrium rate constant of the pseudo-first-order model; and k2 (g/(mg·min)) is the equilibrium rate constant of the pseudo-second-order model.

Fig. 6B and 6C illustrate the fitting curves for the pseudo-first-order and pseudo-second-order kinetic models, respectively, with the relevant fitting results summarized in Table 3. Comparative analysis shows that the correlation coefficient (R2=0.992) for the pseudo-second-order model is much higher than that of the pseudo-first-order model (R2=0.939). Furthermore, the theoretical adsorption capacity calculated from the pseudo-second-order model (101.01 mg/g) is very close to the experimental value (101.3 mg/g). Therefore, the adsorption process of Pb^{2+} by N-MCM-41 follows the pseudo-second-order kinetic model, indicating that chemisorption is the dominant mechanism [29]. This suggests that the interaction between the surface functional groups of N-MCM-41 and Pb^{2+} in aqueous solution is key to achieving effective adsorption.

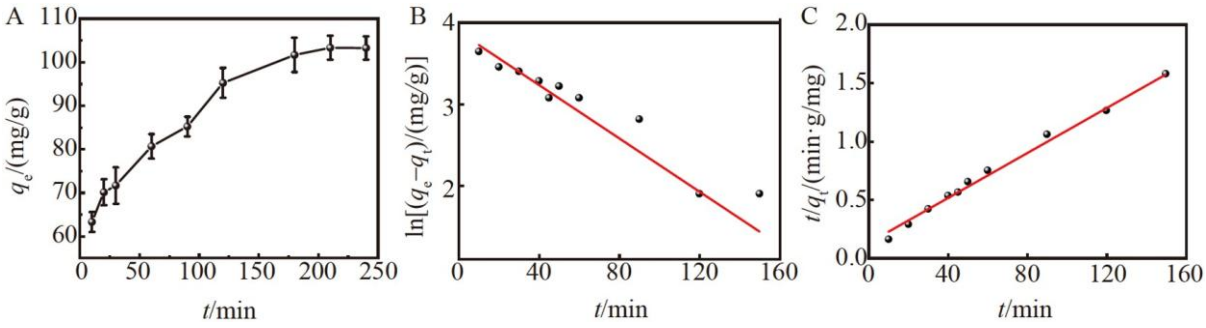

Figure 6 (A) Effect of time on adsorption capacity of N-MCM-41 to Pb2+; (B) Pseudo-first-order adsorption kinetic model; (C) Pseudo-second-order adsorption kinetic model

Table 3 Kinetic parameters for Pb^{2+} adsorption using N-MCM-41.

T / K	qe(exp)/ (mg/g)	k1/ min^{-1}	qe(cal)/ (mg/g)	R2(Pseudo-first-order)	k2/ (g/(mg·min))	qe(cal)/ (mg/g)	R2(Pseudo-second-order)
318	101.3	0.013	44.27	0.939	8.374×10^{-4}	101.01	0.992

3.2.3 Adsorption Thermodynamics

The influence of temperature (298–318 K) on the adsorption process was investigated under the following conditions: solution pH = 5.5, N-MCM-41 dosage = 15 mg, adsorption time = 180 min, and Pb^{2+} concentration = 80 mg/L. The Gibbs free energy change (ΔG, kJ/mol), enthalpy change (ΔH, kJ/mol), and entropy change (ΔS, J/(mol·K)) were calculated using formulas (6)–(9):

$$K_c = \frac{q_e}{C_e} \tag{6}$$

$$\ln K_c = \frac{\Delta S}{R} - \frac{\Delta H}{RT} \tag{7}$$

$$\Delta G = \Delta H - T\Delta S \tag{8}$$

$$\Delta G = -RT\ln K_c \tag{9}$$

Where Kc is the distribution coefficient, T(K) is the absolute temperature, and Ris the ideal gas constant (8.314 J/(mol·K)).

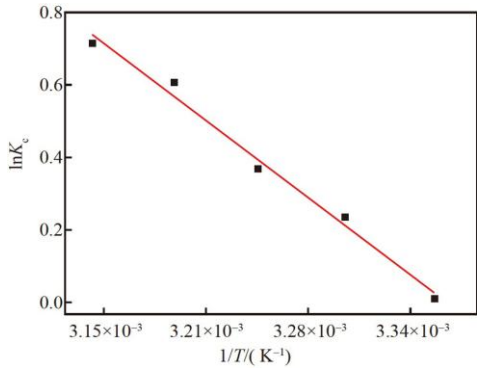

Figure 7 Fitted curve of adsorption thermodynamic model of N-MCM-41 toward Pb^{2+}.

Fig. 7 shows the fitted curve of the adsorption thermodynamic model for N-MCM-41 toward Pb^{2+}, and the relevant thermodynamic parameters are listed in Table 4. The calculation results indicate that during the adsorption of Pb^{2+} by N-MCM-41, ΔGis negative at all tested temperatures, and its value decreases with increasing temperature. This suggests that the adsorption process is spontaneous and that higher temperatures favor the adsorption of Pb^{2+} by N-MCM-41, which is consistent with the results from the adsorption isotherm analysis. Furthermore, both ΔHand ΔSare positive, indicating that the adsorption of Pb^{2+} by N-MCM-41 is an endothermic and entropy-increasing process [30].

Table 4 Thermodynamic parameters of Pb^{2+} adsorbed by N-MCM-41.

T / K	ΔG/ (kJ/mol)	ΔH/ (kJ/mol)	ΔS/ (J/(mol·K))
298	–0.0604		
303	–0.5331		
308	–1.0058	28.129	94.0
313	–1.4786		
318	–1.9513		

3.2.4 Comparison of Adsorption Performance

A comparison of the adsorption performance of unmodified MCM-41 and N-MCM-41 toward Pb^{2+} is presented in Table 5. The adsorption capacity of MCM-41 for Pb^{2+} was only 12.1 mg/g, as the direct adsorption process relies mainly on physical adsorption via its inherent pore structure. After modification with 2-pyridine formaldehyde, the adsorption capacity of N-MCM-41 for Pb^{2+} increased significantly to 101.3 mg/g. This fully demonstrates that the Schiff base modification process in this study effectively endowed MCM-41 with highly efficient adsorption active sites. Comparing the adsorption capacities of different modified MCM-41 adsorbents reported in recent literature (Table 5), N-MCM-41 exhibits a relatively high adsorption capacity for Pb^{2+}, indicating its promising application prospects in treating lead-containing wastewater.

Table 5 Comparison of adsorption performance of different adsorbents toward Pb^{2+}.

Adsorbent	**qe/ (mg/g)**	**t / min**	**Ref.**
CS/MCM-41	90.19	40	[31]
Aminopropyl-MCM-41	64.21	240	[32]
c-MCM-41(40)	58.50	50	[33]
NH_2-MCM-41	57.74	120	[34]
MCM-41-BA	34.20	120	[35]
MCM-41	12.1	120	This work
N-MCM-41	101.3	180	This work

3.2.5 Adsorption Mechanism

To further elucidate the interaction mechanism between N-MCM-41 and Pb^{2+}, XPS was employed to investigate the surface chemical states of N-MCM-41 before and after Pb^{2+} adsorption. Fig. 8A shows the XPS full survey spectra of N-MCM-41 before and after Pb^{2+} adsorption. After adsorption, characteristic peaks of Pb appeared at 138.7 eV and 143.7 eV (Fig. 8B), corresponding to Pb $4f_{7/2}$ and Pb $4f_{5/2}$, respectively [36], indicating the successful adsorption of Pb^{2+} by N-MCM-41. This is consistent with the EDX analysis results (Fig. 8E). Fig. 8C displays the C 1s spectra of N-MCM-41 before and after Pb^{2+} adsorption. Before adsorption, three peaks were observed at 284.5 eV (C-C/C=C), 285.8 eV (C-N), and 287.1 eV (C=N) [37]. After adsorption, the binding energies of the C-N and C=N peaks shifted to 286.0 eV and 287.8 eV, respectively. Fig. 8D shows the N 1s spectra of N-MCM-41 before and after Pb^{2+} adsorption. After adsorption, the N 1s binding energy increased, shifting from 398.7 eV (C-C=N/C-N) and 399.7 eV (-NH_2) [38] to 399.5 eV and 401.2 eV, respectively. This shift is attributed to the lone pair electrons provided by the N atoms entering the empty orbitals of Pb atoms to form coordination bonds with Pb^{2+}, which reduces the electron cloud density around the N atoms, thereby increasing the binding energy. The aforementioned XPS characterization results strongly confirm that chelation and coordination occurred between the surface functional groups of N-MCM-41 and Pb^{2+} during the adsorption process.

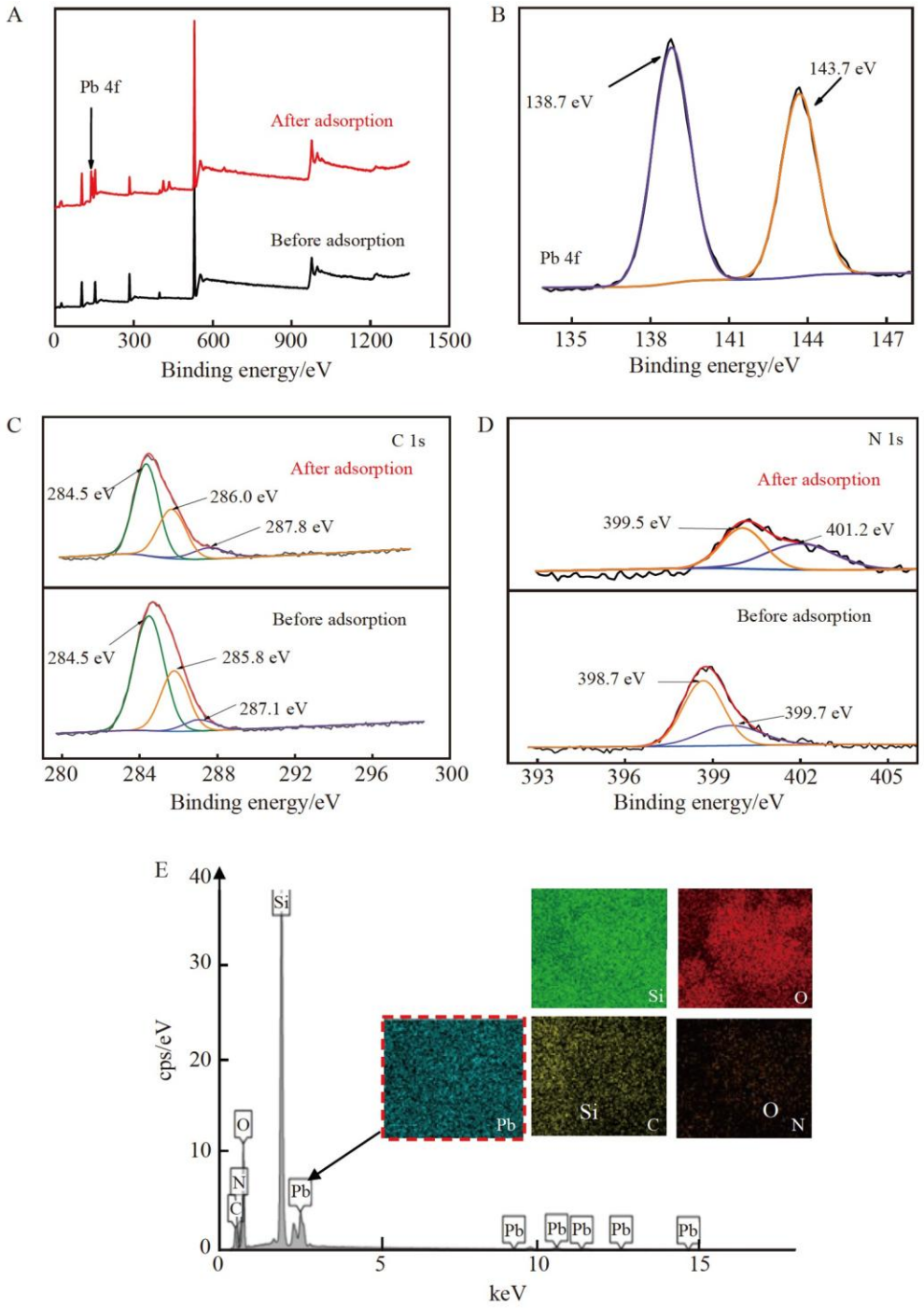

Figure 8 XPS survey spectra (A); Pb 4f spectrum (B); C 1s spectrum (C); N 1s spectrum (D); EDX analyses (E) of N-MCM-41 before and after adsorption of Pb2+

3.2.6 Regenerability and Adsorption Selectivity of the Adsorbent

The Pb^{2+}-loaded sample was placed in a 0.1 mol/L HCl solution, stirred at room temperature for 3 h, centrifuged, dried, and then subjected to another adsorption experiment. The results are shown in Fig. 9A. After five reuse cycles, the adsorption capacity of N-MCM-41 decreased. This is mainly because after multiple adsorption-desorption cycles, some residual Pb^{2+} remained adsorbed on the inner walls of the N-MCM-41 pores, occupying adsorption sites within the pore channels and leading to a decline in performance, which is consistent with the pore structure analysis results (Table 6). However, the adsorption capacity only decreased by 19.73%, indicating

that N-MCM-41 possesses good recyclability. To investigate the adsorption selectivity of N-MCM-41 in bimetallic solution systems, its adsorption performance toward Pb^{2+}/Fe^{2+} and Pb^{2+}/Cu^{2+} was tested, with both the Pb^{2+} concentration and the other metal ion concentrations set at 80 mg/L (Fig. 9B). The results show that although the adsorption performance of N-MCM-41 decreased slightly in the presence of Fe^{2+} and Cu^{2+}, it still maintained a high adsorption capacity for Pb^{2+} (>80 mg/g), indicating that N-MCM-41 has good adsorption selectivity for Pb^{2+}.

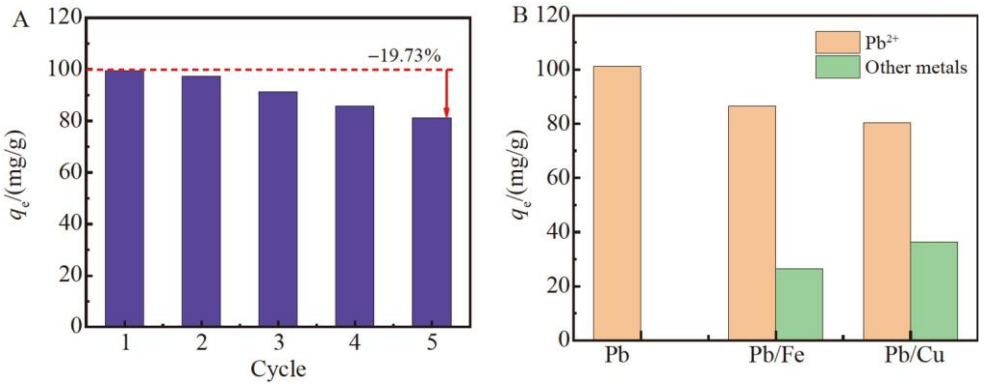

Figure 9 Regeneration performance (A) and adsorption selectivity (B) of N-MCM-41 adsorbent

The exceptional Pb^{2+} adsorption performance of the Schiff base-modified MCM-41 molecular sieve (N-MCM-41) originates from the synergistic integration of its well-preserved mesoporous architecture and the targeted chelation chemistry of grafted 2-pyridine formaldehyde ligands, which collectively overcome the limited affinity of pristine MCM-41 for heavy metal ions. Structurally, the post-grafting modification strategy preserves the intrinsic two-dimensional hexagonal p6mmsymmetry of MCM-41, as confirmed by the persistence of (100), (110), and (200) diffraction peaks in XRD patterns and the retention of ordered pore channels in TEM images. While nitrogen adsorption–desorption analysis reveals a reduction in specific surface area (from 1392.92 to 734.10 m^2/g), pore volume (from 1.02 to 0.43 cm^3/g), and average pore size (from 2.95 to 2.64 nm) post-modification, these changes directly corroborate the successful anchoring of organic ligands within the mesopores rather than pore blockage, ensuring continued accessibility of active sites. The grafting process proceeds via a two-step cascade: first, 3-aminopropyltrimethoxysilane (APTMS) introduces primary amine ($-NH_2$) groups onto the MCM-41 surface via siloxane condensation, yielding NH_2-MCM-41; subsequently, 2-pyridine formaldehyde undergoes a Schiff base condensation with these amines, forming stable imine (-C=N-) linkages and introducing pyridyl moieties as dual coordination sites. Spectroscopic evidence robustly validates this functionalization: FT-IR spectra exhibit new characteristic peaks at 1652 cm^{-1} (-C=N- stretching) and 1442 cm^{-1} ($-CH_2-CH_2-$ scissoring), while XPS surveys detect a distinct N 1s peak at 399.5 eV, with high-resolution N 1s spectra resolving contributions from both imine (C=N) and residual amine ($-NH_2$) groups. Thermogravimetric analysis further quantifies the organic loading, showing an 18.6% total weight loss for N-MCM-41 versus only 7.5% for pristine MCM-41, with 16.1% of this loss attributed to the thermal decomposition of grafted Schiff base ligands between 200 and 800 °C.

The adsorption mechanism is dominated by chemisorption via multi-site chelation and coordination, as conclusively demonstrated by kinetic, isotherm, and XPS analyses. Kinetic studies reveal that Pb^{2+} uptake follows a pseudo-second-order model (R^2 = 0.992), with a calculated equilibrium capacity (101.01 mg/g) nearly identical to the experimental value (101.3 mg/g), confirming chemisorption as the rate-determining step. Isotherm modeling further supports a monolayer adsorption process, with the Langmuir model providing superior fits (R^2 = 0.995 at 318 K) compared to the Freundlich model, and a theoretical maximum capacity (106.95 mg/g) closely matching experimental observations. Thermodynamically, the process is spontaneous (ΔG = -1.95 kJ/mol at 318 K), endothermic (ΔH = 28.13 kJ/mol), and entropy-driven (ΔS = 94.0 J/(mol·K)), consistent with the dehydration of Pb^{2+} ions upon coordination and the increased disorder at the solid–solution interface. XPS analysis of N-MCM-41 post-adsorption provides direct mechanistic insight: the emergence of Pb $4f_{7}/_{2}$ (138.7 eV) and Pb $4f_{5}/_{2}$ (143.7 eV) peaks confirms Pb^{2+} immobilization, while systematic shifts in C 1s and N 1s binding energies reveal electron density redistribution upon coordination. Specifically, the C=N peak shifts from 287.1 to 287.8 eV, and

the C-N/pyridyl N peak shifts from 398.7 to 399.5 eV, indicating that lone electron pairs on both imine nitrogen and pyridyl nitrogen donate electron density into empty 6s/6p orbitals of Pb^{2+}. This dual-site coordination forms stable five- or six-membered chelate rings, significantly enhancing binding strength compared to single-site interactions. The hierarchical pore structure complements this chemistry by facilitating rapid Pb^{2+} diffusion to interior active sites, while the mesoporous framework maintains structural integrity during adsorption–desorption cycles. Collectively, these features elevate N-MCM-41's adsorption capacity to 101.3 mg/g—over eight times higher than unmodified MCM-41 (12.1 mg/g)—surpassing many reported functionalized mesoporous adsorbents and positioning it as a high-performance candidate for Pb^{2+} sequestration.

Table 6 Textural properties of N-MCM-41 before and after adsorption of Pb^{2+}.

Sample	**SBET/ (m^2/g)**	**Pore volume / (cm^3/g)**	**Pore size / nm**
N-MCM-41	734.10	0.43	2.64
Pb^{2+}-N-MCM-41	712.55	0.41	2.46

While N-MCM-41 demonstrates remarkable Pb^{2+} adsorption capacity, selectivity, and recyclability, several critical avenues warrant further exploration to advance its transition from laboratory validation to practical water treatment applications. First, the current study focuses exclusively on single-metal systems; future work should rigorously evaluate adsorption performance in complex real-world matrices containing competing cations (e.g., Ca^{2+}, Mg^{2+}, Na^{+}), natural organic matter (e.g., humic acid), and varying pH levels, as these factors can significantly alter adsorption thermodynamics and kinetics. Expanding investigations to multicomponent heavy metal systems (e.g., Pb^{2+}/Cu^{2+}/Cd^{2+}/Zn^{2+}) will further elucidate the adsorbent's selectivity mechanisms and inform its applicability in diverse contaminated waters, such as acid mine drainage or industrial effluents. Second, the regeneration protocol employing 0.1 mol/L HCl, while effective, may gradually hydrolyze siloxane bonds or cleave Schiff base linkages over extended cycles; thus, optimizing milder desorption agents (e.g., dilute organic acids, chelating agents like EDTA at lower concentrations) or developing pH-responsive desorption strategies could enhance long-term structural stability and reduce secondary waste generation. Third, scaling up synthesis from bench-top batches to pilot-scale production presents challenges in maintaining uniform ligand grafting and preserving mesoporous order; continuous flow synthesis methods or microwave-assisted grafting could improve reproducibility and reduce processing time compared to conventional reflux approaches. Fourth, integrating N-MCM-41 into practical filtration systems—such as packed-bed columns, membrane hybrids, or granular composites—requires balancing adsorption kinetics with hydraulic permeability, as fine powders may cause pressure drops or require post-filtration recovery. Encapsulating N-MCM-41 within alginate beads, polyacrylamide hydrogels, or electrospun polymer fibers could improve handling while retaining accessibility to active sites. Fifth, mechanistic studies would benefit from advanced in situ characterization techniques, such as in situ XPS or EXAFS (Extended X-ray Absorption Fine Structure), to track real-time coordination geometry changes during adsorption, and DFT (Density Functional Theory) calculations to quantify binding energies of Pb^{2+} with imine/pyridyl sites, providing atomic-level insights into selectivity trends. Additionally, assessing the environmental fate of the adsorbent—including potential leaching of grafted ligands or framework silicon under variable environmental conditions—is critical for evaluating ecological safety prior to field deployment. Finally, techno-economic analysis comparing N-MCM-41 with commercial adsorbents (e.g., activated carbon, ion-exchange resins) in terms of raw material costs, synthesis energy input, regeneration efficiency, and service life will clarify its economic viability for large-scale implementation. By addressing these fundamental and applied research gaps, N-MCM-41 can evolve from a promising laboratory material into a robust, cost-effective technology for mitigating lead contamination in global water supplies, contributing to sustainable environmental remediation efforts aligned with circular economy principles.

4 Conclusion

A novel Schiff base-modified MCM-41 molecular sieve (N-MCM-41) was successfully prepared by grafting 2-pyridine formaldehyde onto MCM-41 molecular sieves via a Schiff base reaction. The adsorption performance of N-MCM-41 toward Pb^{2+} was investigated. The maximum adsorption capacity of N-MCM-41 for Pb^{2+} reached 101.3 mg/g. The adsorption process conformed to the Langmuir isotherm model and the pseudo-second-order

kinetic model, characterizing it as a spontaneous, entropy-increasing, and endothermic process. The adsorbent exhibited good regenerability, retaining 80.27% of its initial adsorption capacity after five adsorption-desorption cycles. Furthermore, the adsorbent demonstrated excellent adsorption selectivity for Pb^{2+}. XPS analysis revealed that chelation and coordination occurred between the surface functional groups of N-MCM-41 and Pb^{2+}, which accounts for the excellent adsorption performance. This study provides a valuable reference for the development of efficient and economical adsorbents for heavy metal ions.

References

[1] BILGIN A, ATEŞ E. Water Air Soil Pollut. , 2021, 232(11): 470.
[2] LI D, ZHANG Q, SUN D, YANG C, LUO G. Environ. Sci. Pollut. Res. , 2022, 29(56): 84113-84124.
[3] YAO N, LI C, YU J, XU Q, WEI S, TIAN Z, YANG Z, YANG W, SHEN J. Sep. Purif. Technol. , 2020, 236: 116278.
[4] LI Y, PAN Y, LI B, WANG L, XIAO H. J. Agric. Food Chem. , 2020, 68(18): 5076-5085.
[5] MOOSAZADE M, ASHOORI R, MOGHIMI H, AMANI M A, FRONTISTIS Z, TAHERI R A. Water, 2021, 13(21):3136.
[6] AYANGBENRO A S, BABALOLA O O, AREMU O S. Chemosphere, 2019, 231: 113-120.
[7] MAITY S, PATIL P B, SENSHARMA S, SARKAR A. Chemosphere, 2022, 307: 136115.
[8] YUAN Y, AN Z, ZHANG R, WEI X, LAI B. J. Clean. Prod. , 2021, 293: 126215.
[9] ZHAO H, OUYANG X K, YANG L Y. J. Mol. Liq. , 2021, 324: 115122.
[10] GUO Y, WU D F, WU H M, LIU X Y, XU H Z, CHEN Q Q. Mater. Today Sustainability, 2022, 20: 100212.
[11] ELFEGHE S, SHENG Q, ZHANG Y. ACS Omega, 2022, 7(15): 13042-13049.
[12] AHMED M O, SHRPIP A, MANSOOR M. Processes, 2020, 8(2): 246.
[13] WU H, XIAO Y, GUO Y, MIAO S, CHEN Q, CHEN Z. Microporous Mesoporous Mater. , 2020, 292: 109754.
[14] ZHANG Y, WU G, YANG Y, SUN J, ZHANG D. J. Sol. Gel Sci. Technol. , 2021, 98(1): 170-182.
[15] LIANG H, CHAI K, SHEN F, HE H, HE G, CHEN C, WEI Z. Microporous Mesoporous Mater. , 2023, 351: 112476.
[16] LOLAGE M, CHASKAR M, GHOSH A. J. Porous Mater. , 2021, 28(6): 1867-1879.
[17] SONG X L, QU P, JIANG N, YANG H M, QIU G Z. Colloid. Surf. , A, 2008, 313: 193-196.
[18] LIN Y W, LEE W H, LIN K L, CHENG T W, KUO B Y. J. Mater. Cycles Waste Manage. , 2022, 24(3): 1009-1019.
[19] BERNAL Y P, ALVARADO J, JUÁREZ R L, ROJAS M A M, DE VASCONCELOS E A, DE AZEVEDO W M, INIESTA S A, CAB J V. Optik, 2019, 185: 429-440.
[20] FELLENZ N, PEREZ-ALONSO F J, MARTIN P P, GARCÍA-FIERRO J L, BENGOA J F, MARCHETTI S G, ROJAS S.Microporous Mesoporous Mater. , 2017, 239: 138-146.
[21] LIU C, JIN R N, OUYANG X, WANG Y G. Appl. Surf. Sci. , 2017, 408: 77-87.
[22] FERNANDES G J T, CORIOLANO A C F, SILVA J B, CASTRO F L, FERNANDES V, ARAUJO A S. J. Therm. Anal.Calorim. , 2018, 131(1): 691-695.
[23] ZHANG Yang, LI Lai-Sheng, CHENG Biao-Ping, ZHOU Ren-Dan, NIE Gui-Zhen. Chin. J. Anal. Chem. , 2014, 42(3):375-383.
[24] LIU N, KARUNAKARAN C, LAHLALI R, WARKENTIN T, BUECKERT R A. Planta, 2019, 249(2): 601-613.
[25] KAUR I, KAUR N, SINGH B P, KUMAR R, CHAWLA J. Toxin Rev. , 2021, 41(2): 551-563.
[26] RADI S, TIGHADOUINI S, BACQUET M, DEGOUTIN S, JANUS L, MABKHOT Y N. RSC Adv. , 2016, 6(86): 82505-82514.
[27] YU Hui, CHEN Yan-Fei, GUO Hui-Qin, MA Wen-Tian, LI Jing, ZHOU Shui-Gen, LIN Sen, YAN Liu-Shui, LI Ke-Xin.Chin. J. Anal. Chem. , 2019, 47(11): 1776-1784.
[28] XIAO Yu, GUO Yu, WU Hong-Mei, JIANG Xiao-Qing. Chem. Ind. Eng. Prog. , 2020, 39(1): 257-266.
[29] CHEN Peng, LI Rong, CHEN Bin. Chin. J. Anal. Chem. , 2022, 50(2): 300-309.
[30] GUO Y, XIAO Y, WU H, XU J, CHEN Q. J. Chem. Technol. Biotechnol. , 2021, 96(6): 1709-1719.
[31] GUO Y, LIU D, ZHAO Y, GONG B, GUO Y, HUANG W. J. Taiwan Institute Chem. Eng. , 2017, 71: 537-545.
[32] DU D P, HIEU N T, TO T C, BACH L G, TINH M X, MAU T X, KHIEU D Q. Adv. Mater. Sci. Eng. , 2019, 2019: 8573451.
[33] ZHU W, WANG J, WU D, LI X, LUO Y, HAN C, MA W, HE S. Nanoscale Res. Lett. , 2017, 12(1): 323.
[34] HEIDARI A, YOUNESI H, MEHRABAN Z. Chem. Eng. J. , 2009, 153(1-3): 70-79.
[35] LIU Z S, LI W K, HUANG C Y. Waste Manage. , 2014, 34(5): 893-900.
[36] LAI H, DENG J, WEN S, LIU Q. Miner. Eng. , 2019, 144: 106035.

[37] LIU J, HUANG Z, CHEN Z, SUN J, GAO Y, WU E. J. Clean. Prod. , 2020, 257: 120322.
[38] NGUYEN C H, FU C C, CHEN Z H, TRAN T T V, LIU S H, JUANG R S. Microporous Mesoporous Mater. , 2021, 311:110733.